

Nematic Films and Radially Anisotropic Delaunay Surfaces

Bryan Gin-ge Chen and Randall D. Kamien

Department of Physics and Astronomy, University of Pennsylvania, Philadelphia PA 19104-6396

Received: date / Revised version: date

Abstract. We develop a theory of axisymmetric surfaces minimizing a combination of surface tension and nematic elastic energies which may be suitable for describing simple film and bubble shapes. As a function of the elastic constant and the applied tension on the bubbles, we find the analogues of the unduloid, sphere, and nodoid in addition to other new surfaces.

PACS. 61.30.-v Liquid Crystals – 82.70.Rr Aerosols and foams – 47.55.D Drops and bubbles

1 Introduction and Summary

Composed of elemental air and water with a dash of soap, bubbles and foams are fodder for studies in geometry, topology, and assembly. Understanding their structure and dynamics is essential for many aspects of industrial processing, flow control, and clean drains. The description of bubbles follows geometrically simple laws: a single bubble forms a sphere to minimize its area for fixed volume. When multiple bubbles come into contact, their interfaces obey a set of rules, first suggested by Plateau in 1873 [1] and later proven by Taylor in 1974 [2]. These laws, simple and universal, state that at every edge joins three faces (at 120°) and every vertex joins four edges (at $\cos^{-1}(-1/3) \approx 109.47^\circ$). While the angles are set by simple force balance, the number of faces-per-edge and edges-per-vertex is fixed by area minimization – to change these numbers (3 and 4) would require increasing the total area. Thus, in some sense, the foam problem is “pure” – there are no coupling constants or ratios of parameters that determine the ideal bubble shape. In this paper we study a simple generalization, in principle realizable in soft matter systems: namely, we add in-plane nematic order to the foam. Are there more general rules for these more complicated materials or do the shapes depend critically on a new length scale made from the surface tension and Frank elastic constants? We conclude that not only are the shapes different quantitatively, but that the whole “phase diagram” of shapes as a function of applied tension is dramatically changed. The nematic order is able to support a much richer class of shapes in addition to the classical constant mean curvature Delaunay surfaces: the sphere, unduloid, and nodoid.

Ultimately, we would like to predict the scaling behavior of these so-called nematic foams with time as they coarsen, in analogy with the standard work beginning with Lemlich for normal foams [3, 4, 5]. There it has been found that the average bubble size $\langle R \rangle \sim t^{1/2}$, compatible with

experimental results. In preliminary experiments on liquid crystal foams [6] it was suggested that $\langle R \rangle \sim t^{0.2}$. This difference from the usual coarsening exponent was suggested to be a consequence of defects on the surfaces. In order to study the nematic foam, we will here concentrate on the geometry of general axisymmetric surfaces stationary under a sum of surface tension and nematic elastic energies. In a future paper, we will consider the dynamics of a double bubble system under diffusion [7]. We begin by deriving a functional for this system, then examine single bubble shapes, primarily the generalization of axisymmetric constant mean curvature surfaces, known as Delaunay surfaces.

The functional we consider is simply that of the Frank free energy of an axisymmetric area-minimizing surface with director field along latitude lines:

$$S[r(z)] = 2\pi \int_0^{z_1} dz \left[\left(\gamma + \frac{K}{r^2} \right) r \sqrt{1 + \dot{r}^2} - \frac{p}{2} r^2 \right] \quad (1)$$

We consider the minimizers of this functional as generalizations of Delaunay surfaces. The Delaunay surfaces minimize the following functional, which consists of a surface tension term and a pressure term:

$$S[r(z)] = 2\pi \int_0^{z_1} dz \left[\gamma r \sqrt{1 + \dot{r}^2} - \frac{p}{2} r^2 \right] \quad (2)$$

Minimization of (2) leads to the Young-Laplace law, $p = 2\gamma H$, where H is the mean curvature of the interface.

Our generalization of Plateau’s problem is in a different direction than what has been studied. Unlike the work done on surfaces in external fields (e.g. drops and crystals in a gravitational field) [8, 9, 10], our anisotropy arises spontaneously through the nematic director. Further, our functional depends on an internal degree of freedom and not the extrinsic geometry of the bubble as in the Wulff model [11, 12]. Previous work on fluid membranes with in-plane order have focused on shape transitions [13, 14]

forced in by topology, not curvature. There has been work on the Canham-Helfrich membrane model similar in spirit to our work [15]. Other seminal work includes the study of nematic order on rigid membranes [16]. Our study of bubble shapes complements work on buckling due to defects [17] and vesicle shape due to tilt order [18] – there the energetics and behavior near defects was the focus. Here, we find a class of shapes when the curvature energy is highly anisotropic.

In the next section we will expand on our model and study an even more general class of free energy functionals. We analyze these models and determine whether we have nodoids, unduloids, or bubbles as we vary both the elastic constant and the applied tension along z . In section 3 we describe the actual axisymmetric shapes having reduced their profile to tabulated functions. In section 4 we focus on the free bubble with no applied tension. We conclude with section 5, the conclusion.

2 The Model

In this section we put together the requisite energetic contributions to derive an energy functional for a thin nematic liquid crystalline film without any translational order. An ordinary soap film is modeled by a surface $S \subset \mathbb{R}^3$, which minimizes:

$$F_A = \gamma \int_S dA \quad (3)$$

where γ is the surface tension. With a volume constraint, the stationary points of this free energy are constant mean curvature (CMC) surfaces which obey the Young-Laplace Law, $\Delta p = 2\gamma H$, where Δp is the pressure jump across the interface and H is its mean curvature. In the absence of any volume constraints we have $H = 0$ and the surface tension does not play a role in the ground state structure. As Veit Elser has put it, this problem of minimal surfaces is “pure” – it does not depend on any particular interactions or elastic constants [19]. Here we aim to minimally embellish the physics of minimal and CMC surfaces. We add a nematic director \mathbf{n} , obliged to lie in the surface, and include its Frank free energy [20]:

$$F = \frac{1}{2} \int d^3x \left\{ K_1 (\nabla \cdot \mathbf{n})^2 + K_2 [\mathbf{n} \cdot (\nabla \times \mathbf{n})]^2 + K_3 [\mathbf{n} \times (\nabla \times \mathbf{n})]^2 \right\} \quad (4)$$

where K_1 , K_2 , and K_3 are the splay, twist, and bend elastic constants, respectively. When restricted to a thin film of thickness $h \sim kT/K_i$ with planar boundary conditions on the inner and outer surfaces, the director will be independent of the depth in the film and we may treat it as a two-dimensional line field in the tangent plane of the surface, S .

When the nematic director lies in a surface, the twist term vanishes; without loss of generality we work in the

tangent plane to an arbitrary point so that the director is $\mathbf{n} = (n_x, n_y, 0)$, and the normal is in the z direction. Then

$$\begin{aligned} \mathbf{n} \cdot [\nabla \times \mathbf{n}] &= n_x (\partial_z n_y - \partial_y 0) + n_y (\partial_x 0 - \partial_z n_x) \\ &\quad + 0 (\partial_x n_y - \partial_y n_x) \\ &= 0 \end{aligned} \quad (5)$$

since \mathbf{n} is independent of z at this point. Thus the twist term vanishes and the bend term is simply $(\nabla \times \mathbf{n})^2$.

In addition to the difference between splay and bend $K_1 - K_3$, the surface normal \mathbf{N} breaks the bend term into two rotationally-invariant pieces. Defining $\mathbf{t} \equiv \mathbf{n} \times (\nabla \times \mathbf{n})$, we have two scalars, $t_N = \mathbf{N} \cdot \mathbf{t}$ and $t_\perp = |\mathbf{t}| - t_N$. These two types of bend can each have a different elastic cost for bend in the surface and out of the surface, K_{3N} and $K_{3\perp}$, respectively. The free energy contribution from the nematic is:

$$F_n = \frac{h}{2} \int_S dA \left\{ K_1 (\nabla \cdot \mathbf{n})^2 + K_{3N} t_N^2 + K_{3\perp} t_\perp^2 \right\} \quad (6)$$

Note that this is, in principle, a functional of both the shape of the surface and the director field living on it. We will focus on this interplay in the following.

Recall that Delaunay surfaces are CMC surfaces of revolution. In order to generalize these for nematic films, we will focus on the case where the director field lies parallel to the lines of “latitude” on a surface of revolution. In cylindrical coordinates, (r, ϕ, z) , these are lines of constant z . These configurations are automatically splay-free, further removing the dependence on K_1 . In future work, we will consider the fusion of two such nematic bubbles (i.e. the double-bubble problem [21]) since this line field is consistent with the condition that the director is parallel to the Plateau borders (Fig. 1) [7].

In Cartesian coordinates, the director field at (x, y, z) is $\mathbf{n} = (y, -x, 0)/r$ and the normal is $\mathbf{N} = (x, y, z)/R$, where $r = \sqrt{x^2 + y^2}$ and $R = \sqrt{x^2 + y^2 + z^2}$. Direct calculation confirms that $\nabla \cdot \mathbf{n} = 0$. And

$$\begin{aligned} \mathbf{t} &= \mathbf{n} \times [\nabla \times \mathbf{n}] \\ &= \frac{x\hat{\mathbf{x}} + y\hat{\mathbf{y}}}{r^2} \end{aligned} \quad (7)$$

We have $|\mathbf{t}|^2 = 1/r^2$, $t_N^2 = 1/R^2$ and $t_\perp^2 = (\csc^2 \theta - 1)/R^2$ where θ is the polar angle in polar coordinates.

In keeping with the spirit of minimally modifying the soap bubble problem, we will set $K_{3\perp} = K_{3N} = K_3$ in the proceeding. We shall show that even without the anisotropies of K_1 and $K_{3\perp} - K_{3N}$, the shapes of single surfaces are qualitatively modified by $K_3 \neq 0$. In this limit, the nematic free energy only depends on r , the xy -radius of the film so that

$$F_n = \frac{K_3}{2} \int dA \frac{1}{r^2} \quad (8)$$

Axisymmetric surfaces may be parameterized by the z coordinate so that $\mathbf{R}(z) = [r(z) \cos \theta, r(z) \sin \theta, z]$. The total

free energy as a function of the cylindrical coordinate $r(z)$ parameterizing the surface is

$$F[r(z)] = 2\pi\gamma \int_0^{z_1} dz \left\{ r\sqrt{1+\dot{r}^2} \left(1 + \frac{K}{r^2} \right) - \frac{p}{2}r^2 \right\} \quad (9)$$

where $K \equiv hK_3/\gamma$ with has units of length-squared and the where $p = \Delta P/\gamma$ is the reduced pressure. Taking values for the lyotropic liquid crystal PAA, $K_3 \sim 1.2 \times 10^{-6}$ dynes and its surface tension is ~ 35 dynes/cm [22]. Thicknesses of typical soap films are about four microns. Therefore, $K \sim 1.4 \times 10^{-11}$ cm². This results in a length scale $\sqrt{K} \sim 4 \times 10^{-6}$ cm, which is smaller than the thickness of the film. We point out, however, that in a dry foam, things could be quite different. In particular, since the variation of the area is the mean curvature, H , we expect that after coarsening, H is close to zero. In this regime, the principal curvatures need not vanish and, indeed, our extra term is sensitive to them. We will explore this possibility in a sequel [7] which studies the dynamics of this new class of bubbles. In flowing polymer systems or films with magnetic dipoles, K could be considerably larger; in the mean time, we focus on this new variational problem and show that it leads to novel shapes and geometries, even in this simple limit.

Let's take a step back from our particular model to consider a broader class of functionals. We can write our energy as:

$$F = 2\pi\gamma \int dz \left\{ [1 + Kg(r)] r\sqrt{1+\dot{r}^2} - \frac{p}{2}r^2 \right\} \quad (10)$$

We interpret $1 + Kg(r)$ as a spatially varying surface energy. This is unlike the anisotropic surface energies in the sense of the Wulff construction for crystal shapes, in which the anisotropy refers to a dependence on the direction of the normal vector [11,12]. This energy is spatially varying in r , and has, to our knowledge, not been considered, in contrast to the spatially varying in z case [8,9,10]. Note that $g(r)$ ought to be even as a function of r , in order for there to be the symmetry $r \leftrightarrow -r$. For the case of latitudinal nematic director lines, $g(r) = 1/r^2$.

We will be comparing the properties of surfaces minimizing (strictly speaking, extremizing, as we won't study the second variation) this free energy with the well-studied case of Delaunay surfaces ($K = 0$). In order to give a more complete picture of the properties of surfaces minimizing spatially varying surface tension energies, we will begin by discussing the axisymmetric minimizers of the general family of free energy functionals described by (10). We will call these minimizers "radially anisotropic Delaunay (RAD) surfaces".

Since the integrand is of the form $f(r, \dot{r})$, we may take advantage of the standard first integrals of the calculus of variations. Because f does not depend explicitly on z , (if z were time this would lead to conservation of energy), we have:

$$f - \dot{r} \frac{\partial f}{\partial \dot{r}} = T \quad (11)$$

where T is a constant. This last equation may be interpreted as a conservation of force along the z -axis, with T

an applied tension or compression, depending on its sign. For a free bubble, $T = 0$, which is the analog of the sphere. Setting this to other values will yield RAD surfaces analogous to the other Delaunay surfaces, such as the nodoid and unduloid. We shall see that the types of RAD surfaces that are possible as we vary T will depend on the value of K in a nontrivial way.

If we insert our expression for $f(r, \dot{r})$, we can rewrite (11):

$$\pm \gamma \frac{2\pi r}{\sqrt{1+\dot{r}^2}} [1 + Kg(r)] = T + \pi r^2 \Delta P \quad (12)$$

This is an equation for force balance in the z -direction¹: on the right hand side, the two terms correspond respectively to the applied tension and the pressure-induced force on a surface with xy cross-section πr^2 . Likewise, the left side is the effective surface tension $\gamma[1 + Kg(r)]$ multiplied by the length of the boundary, $2\pi r$. The factor of $\pm(1+\dot{r}^2)^{-1/2}$ projects the z -component of this force. The ambiguity in sign arises from the fact if \dot{r} passes through infinity, the sign of the surface tension force must change as well. In subsequent analysis we will need to be careful about which branch of the radical we choose, in particular in the case of the nodoid where \dot{r} does indeed goes through infinity and the z -component of the tangent vector to the curve changes sign. We will cross that cut when we come to it.

By rewriting for ΔP , we can derive a generalization of the Young-Laplace rule:

$$\Delta P = \frac{2\gamma [1 + Kg(r)]}{r\sqrt{1+\dot{r}^2}} - \frac{T}{\pi r^2} \quad (13)$$

Choosing the film to be symmetric about $z = 0$, we know that $\dot{r}(0) = 0$ and if we define $R = r(0)$, the radius of the "waist" then

$$\Delta P = \frac{2\gamma}{R} [1 + Kg(R)] - \frac{T}{\pi R^2} \quad (14)$$

When K and T both vanish, this reduces to the standard Young-Laplace rule.

En passant we note that in the case of contact between two bubbles, the effective surface tension $\gamma[1 + Kg(r)]$ is *identical* for the three partial caps shown in Fig. 1 since the value of r is the same where they meet. As a result, the triple junction will join the three surfaces at 120°, just as in regular foams. However, the equality of surface tensions is an accident of axisymmetry and in general, Plateau's rules will not hold.

2.1 Families of RAD surfaces

In this section we analyze the families of RAD surfaces as we change T and K . First, let us measure T in units of γ

¹ We note that in the study of CMC surfaces, this is an expression for the magnitude of the weight vector [23], which can be used to show that CMC surfaces must asymptote to Delaunay surfaces at infinity. Whether this notion can be generalized to our problem is an open question.

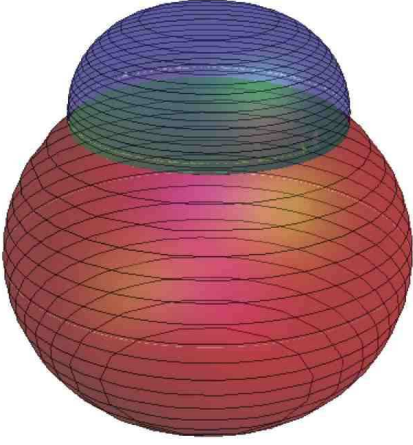


Fig. 1. Double RAD bubble, with $g(r) = 1/r^2$ and $K = 0.01$. Three $T = 0$ caps meet at 120° .

as we did for K and p , i.e. $\bar{T} = T/(\pi\gamma)$. The force balance equation with our radial anisotropy function specialized to $g(r) = 1/r^2$ (the nematic-derived case) now reads

$$\frac{r}{\pm\sqrt{1+\dot{r}^2}} \left(1 + \frac{K}{r^2} \right) - \frac{p}{2} r^2 = \bar{T} \quad (15)$$

If $p \neq 0^2$, we may also scale out the dependence on p via $\tilde{r} = pr/2$, $\tilde{z} = pz/2$, $\tilde{T} = p\bar{T}/2$, and $\tilde{K} = p^2 K/4$:

$$\frac{\tilde{r}}{\pm\sqrt{1+\dot{\tilde{r}}^2}} \left(1 + \frac{\tilde{K}}{\tilde{r}^2} \right) - \tilde{r}^2 = \tilde{T} \quad (16)$$

In the following analyses, we will drop the tilde from our variables unless there is any ambiguity. There remains only one free parameter, K .

We begin the study of the family of RAD surfaces with a given K by viewing $T = T(r, \dot{r})$. In Fig. 2 we have plotted the embedded surfaces $[r, \dot{r}, T(r, \dot{r})]$ for both branches of the radical. Contours of constant T correspond to values of r, \dot{r} on different axisymmetric surfaces with a fixed tension.

We start by considering the positive branch phase portrait first – the features sketched below should be considered as a taste of things to come in our later analysis. The diagram of this branch of the T -surface represents points on the generating curves of RAD surfaces where the tangent vector points upwards (has a positive z -component). In Fig. 3 we have set $K = 0.01$ and find that there are several families of contours which cut across this branch

² We have not examined the $p = 0$ surfaces, but these will be to minimal surfaces as general RAD surfaces are to CMC surfaces, and will hence be a generalization of catenoids.

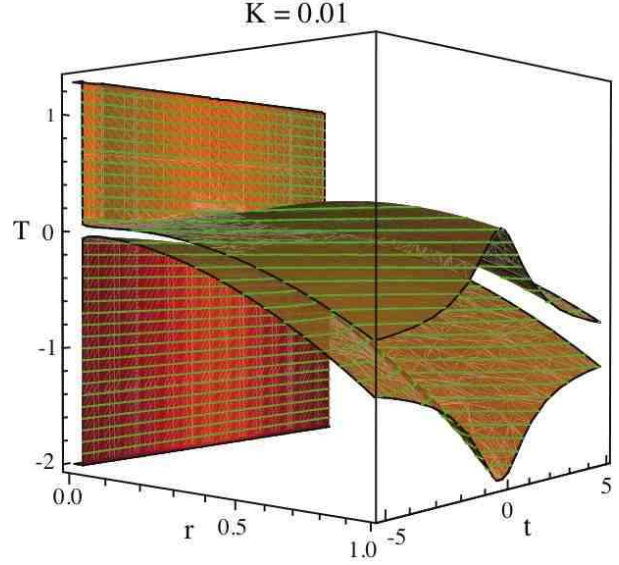


Fig. 2. The surface $T(r, \dot{r})$, when $K = 0.01$. Each connected constant height contour (green) corresponds to r, \dot{r} for a generating curve for a RAD surface.

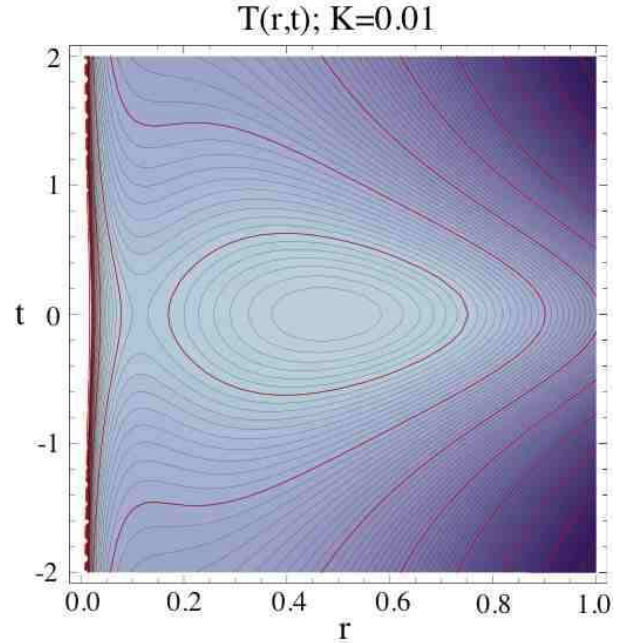


Fig. 3. The constant T contours on the positive branch of $T(r, \dot{r})$. Closed contours correspond to unduloids, the single maximum is a cylindrical solution.

of the T -surface. First, the $T = 0$ contour represents the curve (r, \dot{r}) for a free bubble, indeed, there is a range of T such that the contours imply that $\dot{r} = \pm\infty$ as $r \rightarrow 0$ – these all represent closed bubbles. Note that among these there are those which remain completely on the positive branch (convex bubbles), and some which run to the negative branch (Fig. 4) as well (concave bubbles). There are also closed curves with $T > 0$ on the positive branch which represent solutions periodic in z . These are the so-called

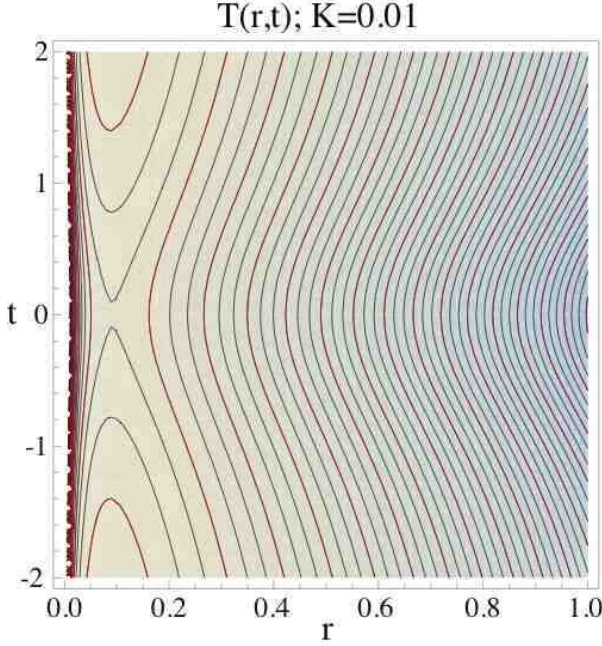


Fig. 4. The constant T contours on the negative branch of $T(r, \dot{r})$. Each contour joins with one on the positive branch as it passes through $\dot{r} = \infty$.

unduloidal solutions. The single point solution is a cylinder (since $r = \text{const}$). Finally, there are also curves with $T < 0$ which “jump” to the negative branch and back, that is $\dot{r} = \pm\infty$ for nonzero r – these are the nodoids, the periodic self-intersecting surfaces, where the tangent vector turns in a loop in each repeat unit. Note that not all surfaces cut the negative branch of the T -surface, but all must cut the positive branch. To see this, note that in (16) when $T > 0$, we must choose the positive branch, while when $T < 0$ we have solutions for both signs of the radical, in particular for large \dot{r} .

This can be generalized for any $g(r)$. Contours of constant T are either closed (unduloids), run off to $\dot{r} = \pm\infty$ at $r = 0$ (bubbles), or run off to $\dot{r} = \pm\infty$ at finite r (nodoids). Here we sketch how to partition the full space of RAD surfaces into these three classes when $g(r)$ is arbitrary by studying the special case $g(r) = 1/r^{2n}$ for $n \in \mathbb{Z}^+$. This corresponds to assigning an energy to the lines of latitude of κ^{2n} , where κ is their curvature in \mathbb{R}^3 , and one of the principal curvatures of the surface. We label the second argument of $T(\cdot, \cdot)$ as $t = \dot{r}$ in the following and will study the function $T(r, t)$.

It’s a fact from the theory of bifurcations in dynamical systems that the critical points of the $T(r, t)$ -surface indicate where the geometry of the contours change, and hence those values of T for which the geometry of the RAD surfaces change. For example, near a local minimum or maximum, the contours of constant T are closed curves encircling the extrema. However, at a saddle point of the T -surface, these closed contours are separated into two groups; the separatrix is a self-intersecting curve and corresponds to a singular topological change in our surface.

Thus, if we find the critical points and their types (minima, maxima, saddle), then each of the families mentioned will correspond to families of contours which lie on points of the surface between the critical points. In order to find the critical points, we calculate the gradient of T and look for its zeros.

$$\nabla T = \pm \left(\frac{1 - K(2n-1)r^{-2n}}{\sqrt{1+t^2}} - 2r, -\frac{rt(1 + Kr^{-2n})}{(1+t^2)^{3/2}} \right)$$

When $\nabla T = 0$,

$$\pm \frac{1 - K(2n-1)r^{-2n}}{\sqrt{1+t^2}} = 2r \quad (17)$$

$$rt(1 + Kr^{-2n}) = 0 \quad (18)$$

Since r is real and positive, we must have $t = 0$ and so all critical points of T must lie on the line $t = 0$. The Hessian H provides information on whether a critical point is a saddle, minimum, or maximum. At $t = 0$

$$H = \begin{pmatrix} \pm 2Kn(2n-1)r^{-2n-1} - 2 & 0 \\ 0 & \mp r(1 + Kr^{-2n}) \end{pmatrix} \quad (19)$$

Since H is diagonal, it is easy to see that the directions of maximum change in T are along the r and t directions with the corresponding eigenvalues on the diagonal of the matrix. Note that on either branch, H_{tt} does not change sign. Thus on the positive branch it is always negative and the $t = 0$ line is ridge-like; similarly on the negative branch the $t = 0$ line is valley-like. Thus our work is simplified since we need only check H_{rr} to determine which type of extrema we have.

As we have discussed, the $T = 0$ solution has significance as the “free” solution with no imposed tension at the boundaries, but is also important in another respect. Solutions with $T > 0$ *cannot* have portions on the negative branch, as then both terms on the left hand side of the force balance equation (15) would be negative. This implies that the $T = 0$ solution lies at the boundary between surfaces which may be parametrized simply as $r(z)$, and those which cannot – a result of the behavior of the z -component of the tangent vector. Luckily, a half-repeat of any surface can be parametrized as $z(r)$, which saves us from having to look at a completely parametric representation $(r(s), z(s))$.

Along the ridges/valleys we have

$$T = \pm r \left(1 + \frac{K}{r^{2n}} \right) - r^2 \quad (20)$$

or

$$(r^{2n} + K)^2 - r^{4n-2} (T + r^2)^2 = 0 \quad (21)$$

We denote r_0 to be the value of $r(z)$ when $dr/dz = t = 0$. All possible values of r_0 are real roots of (21). Letting $u = r^2$, we see that the real roots r_j of the degree $4n+2$ polynomial in r arise from positive real roots u_j of the degree $2n+1$ polynomial in u

$$P(u) = (u^n + K)^2 - u^{2n-1} (T + u)^2 \quad (22)$$

On the T -surface, the points $(r_j, 0)$ are where the contour corresponding to a RAD surface intersects the r -axis. Note that when $T(r_j, 0)$ is a critical point, r_j must be a double root of $P(r_j^2) = 0$. We will use this fact many times in what follows. Though it would be tempting to associate each distinct positive root u_j for fixed T with a distinct RAD surface, a single generating curve may have multiple points where $dr/dz = 0$.

2.2 Reduction to Quadrature

Indeed, while it's simple to examine the picture of the T -surface to see which points are part of the same contour, the mathematics is more subtle. To flesh this out, we take a small detour to integrate our force balance equation by quadratures for the function $z(r)$. Again, there is a sign ambiguity in the integrand, the same sign ambiguity that we have seen throughout. We now set the sign by the boundary condition that z -component of the curve's tangent vector is positive where we begin the integration. We choose the origin along the z -axis at the place where $\dot{r} = 0$. At this place $P(u)$ vanishes, by construction, and we have

$$z(r) - 0 = \int_{r^2(0)}^{r^2} \frac{(T+u) u^{n-1} du}{2\sqrt{(u^n + K)^2 - u^{2n-1}(T+u)^2}} \quad (23)$$

Note that the denominator vanishes as \sqrt{u} near the lower limit and thus the singularity is integrable. Also, since we only integrate between consecutive roots of $P(u)$, the sign of the integrand remains fixed. Of course there are several roots of $P(u)$. Let u_j for $1 \leq j \leq 2k+1$ be a positive real root of $P(u)$, with $0 = u_0 < u_1 \leq \dots \leq u_{2k+1}$, so that $2k+1$ is the total number of real roots (an odd degree equation with real coefficients is guaranteed an odd number of real roots since complex roots must come in conjugate pairs). The values of T , K control the coefficients of $P(u)$ and hence whether $k = 0, 1, \dots, n$. The integral for $z(r)$ can only remain real when $P(u) > 0$ and the intervals of u such that this is true are also bounded by the u_j . Therefore, only for r^2 such that $P(r^2) > 0$ will the integral from u_j to r^2 result in a real valued $z(r)$.

Each interval over which $P(u) > 0$ corresponds to a distinct type of RAD surface. When $K = 0$, the only closed bubble solution is the sphere when $T = 0$. However, when $K \neq 0$, $P(0) = K^2 > 0$ for any T and the first valid interval is $r^2 \in (0, u_1)$. This corresponds to closed bubbles, as $r = 0$ means that the generating curve touches the z -axis. The existence of this interval for $K \neq 0$ therefore means that there will be a closed bubble solution for any T .

To exercise our formalism, we review the well-studied $K = 0$ Delaunay surfaces. Taking $K = 0$ in our equations directly yields

$$\begin{aligned} P(u) &= (u^n + 0)^2 - u^{2n-1}(T+u)^2 \\ &= u^{2n-1} \left[u - (T+u)^2 \right] \end{aligned} \quad (24)$$

We will drop the factor of u^{2n-1} as it yields $2n-1$ degenerate RAD “surfaces” $u = 0$. Then the system is independent of n , and we recover the classical Delaunay surfaces.

In Fig. 5 we plot $T(r, 0)$ versus $\log r$; this is a plot of the cross section of the T -surface through the plane $t = 0$, flipped on its side. This graph is a “tomographic slice” of the a general T -surface like that in Fig. 2 except with $K = 0$. The two branches of the boundary curve are $T(r, 0) = \pm r - r^2$ or, in other words, $u_{\pm}(T) = r_{\pm}^2(T)$ are the solutions to the quadratic equation $P(u) = u - (T+u)^2 = 0$. The region between the two curves satisfies $P(u) > 0$, and has been shaded blue and green, for the periodic surfaces and the closed bubble surface, respectively. The generating curves for Delaunay surfaces are found by setting $K = 0$ in (23), so they are described by

$$z(r) = \int_{u_-}^{r^2} \frac{(T+u)du}{2\sqrt{u}\sqrt{u-(T+u)^2}} \quad (25)$$

where u_- is the smaller root of $P(u)$

$$u_{\pm} = \frac{1}{2} \left(1 - 2T \pm \sqrt{1 - 4T} \right) \quad (26)$$

When $T \leq \frac{1}{4}$, the roots are real and $u_{\pm} > 0$. Moreover, u_- vanishes only for $T = 0$ and so the only closed surface at $K = 0$ is the free, tensionless bubble. One can see easily from $z(r)$ that it is a sphere in this case. Recall that this solution with $T = 0$ separates surfaces with contours that lie entirely on the positive branch of T from those that do not. For the Delaunay surfaces, the difference between the unduloids ($T > 0$) and the nodoids ($T < 0$) is straightforward: the nodoids all self-intersect, and the unduloids do not as shown in Figs. 6 and 7.

When the two roots coincide, the integrand diverges over the integration region unless r^2 is constant and equal to u_{\pm} , i.e. a cylinder. The discriminant of the quadratic equation, $Q(T) = 1 - 4T$ vanishes at this point, and one can also check that $T = 1/4$ is the only critical point on the $T(r, t)$ surface. Since points with $t = 0$ on the positive branch of T are on a ridge, the cylindrical solution is the maximum of T .

Finally, we may study the “period” of the Delaunay surfaces as we change T as a further diagnostic of the resulting bubbles. We define the period as the twice the height between the endpoints of a surface or $Z \equiv 2[z(r_+) - z(r_-)]$, where $r_i^2 = u_i$:

$$\begin{aligned} Z &= \int_{u_-}^{u_+} \frac{(T+u)du}{\sqrt{uP(u)}} \\ &= \int_{u_-}^{u_+} \frac{(T+u)du}{\sqrt{u(u-u_-)(u_+-u)}} \\ &= \frac{2T}{r_+} K \left(\sqrt{1 - \frac{u_-}{u_+}} \right) + 2r_+ E \left(\sqrt{1 - \frac{u_-}{u_+}} \right) \end{aligned} \quad (27)$$

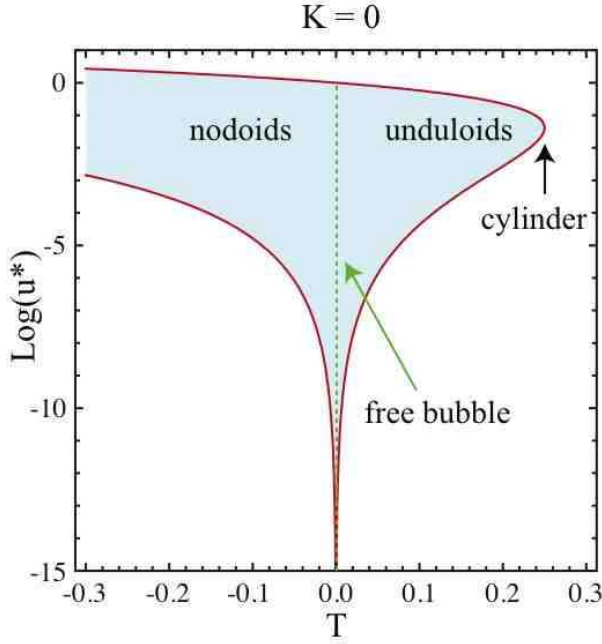


Fig. 5. A log-plot of the $t = 0$ slice through the T -surface for $K = 0$. The shaded portion of the graph maps out the range of $u = r^2(z)$ for each Delaunay surface as a function of T .

valid when $T \leq 1/4$ and where $K(\cdot)$ and $E(\cdot)$ are the complete elliptic integrals of the first and second kind³. As shown in Fig. 14, as $T \rightarrow -\infty$, the period goes to zero (corresponding to tightly wound nodoids), and at $T = 0$, $u_-/u_+ = 0$, $r_+ = 1$ and the period, and hence the diameter of the sphere is 2. As $T \rightarrow 1/4$, the period goes to π . This might be unexpected, as the period of a cylinder ought to be undefined, or perhaps zero or infinite. However, this result just implies that the cylindrical limit is reached by the vanishing of wiggles in the surface, rather than singular behavior in the period function.

Having cut our teeth on the $K = 0$ case, we move on but refer the interested reader to other sources [24, 25]. As we mentioned, an essential difference between the $K = 0$ and $K \neq 0$ case is the possibility of additional *distinct* solutions for fixed T . If $K \neq 0$, we can find new solutions as follows: since $P(u) > 0$ in the interval $(0, u_1)$, and $P(u_1) = 0$, it follows that $P(u) < 0$ for $u \in (u_1, u_2)$. Thus for $r^2 \in (u_2, u_3)$, $P(r^2) > 0$ and we find a new valid solu-

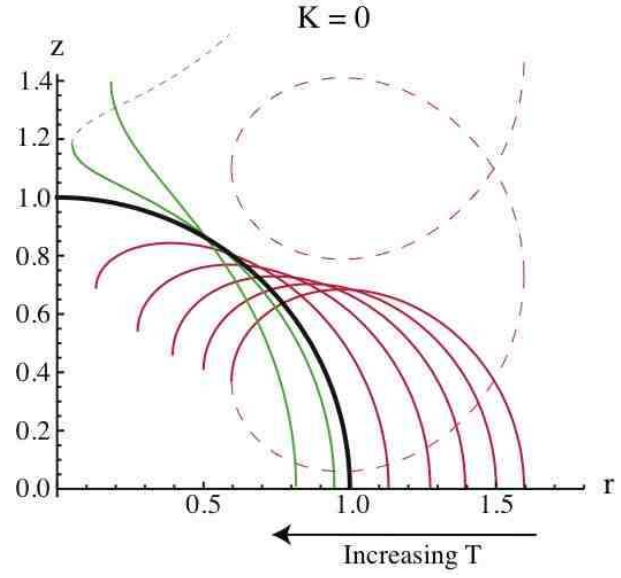


Fig. 6. Generating curves of Delaunay surfaces. Nodoids are red, unduloids are green, and the spherical solution ($T = 0$) is in black. Dashed curves show a few repeats of a nodoid and an unduloid.

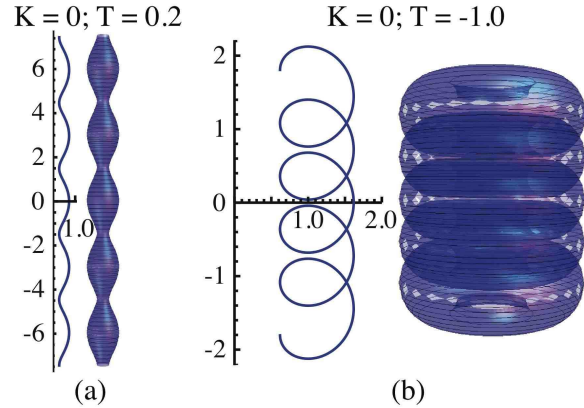


Fig. 7. Comparison of a Delaunay unduloid (a) and nodoid (b), at $T = 0.2$ and $T = -1$ respectively. Note that the loops formed by the self-intersections in (b) point “inwards”, so that this is an example of an “innie” nodoid (c.f. Fig. 17d).

tion of the force balance equation. We may evaluate the integral for $z(r)$ either from r^2 to u_{2j+1} or from u_{2j} to r^2 – the difference will be whether we define the plane $z = 0$ at the “outer radius” or at the “inner radius” of the surface and corresponds only to a shift along z . Continuing with this reasoning we will find distinct surfaces by integrating values of $r^2 \in (u_{2j}, u_{2j+1})$ for $j = 0 \dots k$, so that we have $k + 1$ distinct surfaces.

As mentioned earlier, there is a connection between multiple roots of $P(u)$ and critical points on the T -surface. If there are repeated roots, then by perturbing T slightly, we can interpret the solutions as lying on a separatrix. Depending on the parity of the colliding roots, either two intervals of positive $P(r^2)$ join (when $u_{2j} \rightarrow u_{2j+1}$ for some j) and two families of surfaces join into one, or an

³

$$\begin{aligned}
 F(\phi, k) &= \int_0^\phi \frac{d\theta}{\sqrt{1 - k^2 \sin^2 \theta}} \\
 &= \int_0^{\sin \phi} \frac{dz}{\sqrt{(1 - z^2)(1 - k^2 z^2)}} \\
 E(\phi, k) &= \int_0^\phi \sqrt{1 - k^2 \sin^2 \theta} d\theta \\
 &= \int_0^{\sin \phi} \frac{\sqrt{1 - k^2 z^2} dz}{\sqrt{1 - z^2}}
 \end{aligned}$$

$$\text{and } K(k) = F(\pi/2, k) \text{ and } E(k) = E(\pi/2, k)$$

interval where $P(r^2) > 0$ vanishes and the limits of the integral degenerate into a point and we have an infinite cylinder of radius $r^2 = u_{2j+1} = u_{2j+2}$ for some j .

Therefore, studying the discriminant of $P(u)$, which we call $Q(K, T)$ will reveal how many positive real roots P has, and hence how many distinct RAD surfaces⁴. For simplicity, we specialize to $n = 1$, where

$$\begin{aligned} P(u) &= (u + K)^2 - (T + u)^2 u \\ Q(K, T) &= -(K - T)^2(4K + 27K^2 - 18KT - T^2 + 4T^3) \\ &= -(K - T)^2 Q_3(K, T) \end{aligned} \quad (28)$$

where the last equation defines the cubic factor $Q_3(K, T)$. Since $P(u)$ is cubic, it may have one or three real roots. When the discriminant vanishes, roots collide. This may happen if $K = T$ or at a root of Q_3 . $K = T$ implies that the roots of $P(u)$ are $\{1, -K, -K\}$. When $K > 0$ the repeated root corresponds to non-physical, imaginary values of r and so the vanishing of $Q(T, T)$ is of no particular physical consequence there. We will discuss the $K < 0$ case only briefly at the end of this section. We thus focus on the roots of $Q_3(K, T)$ which are precisely the critical points in T , the values of tension at which there is a crossover between a system where there is one bubble (one real root), and one where we have a bubble and another surface (three real roots). We'll discuss the geometry of these surfaces later.

Moreover, the number and nature of the critical points of T varies as we changed K . Note that as K changes, the positions of the roots of $Q_3(K, T)$ move as well. Hence we may expect that if we tune K through certain critical values, the critical values of T will themselves collide or split, and so we gain or lose entire families of RAD surfaces. It will therefore be of use to consider the discriminant of $Q_3(K, T)$. $K = 0$ will necessarily be a critical value in K because there the stationary surfaces are simply the ordinary Delaunay surfaces along with multiple degenerate $u = 0$ roots in $P(u)$ which we dropped in our discussion above. Since this case is understood, we focus on nonvanishing critical values of K .

Since the relevant factor of the discriminant $Q(K, T)$ is cubic, we may have one or three (real) critical points in T . The discriminant of $Q_3(K, T)$ is

$$D_3 = -16K(-1 + 27K)^3 \quad (29)$$

Descartes rule of signs tells us that $Q_3(K, T)$ will always have one (real) negative root in T , which we label T_1 . If the other two roots are complex, then let $T_2 = T_3^* = \mu + i\nu$. Since $D_3 = 64(T_1 - T_2)^2(T_1 - T_3)^2(T_2 - T_3)^2$ we see that in the case of one real root $D_3 = -256[(T_1 - \mu)^2 + \nu^2]^2 \nu^2 < 0$. When all three roots are real, however, D_3 is real and positive. Thus when $0 < K < 1/27$ there are three critical points, but for larger K there is only one critical point on the T -surface.

⁴ Recall that for a general cubic, $ax^3 + bx^2 + cx + d$ with roots r_1, r_2 , and r_3 , we have $r_1 r_2 r_3 = -d/a$, $r_1 r_2 + r_2 r_3 + r_1 r_3 = c/a$, and $r_1 + r_2 + r_3 = -b/a$. It follows that $b^2 c^2 - 4ac^3 - 4b^3 d - 27a^2 d^2 + 18abcd = a^4(r_1 - r_2)^2(r_1 - r_3)^2(r_2 - r_3)^2$. This is the discriminant of the cubic.

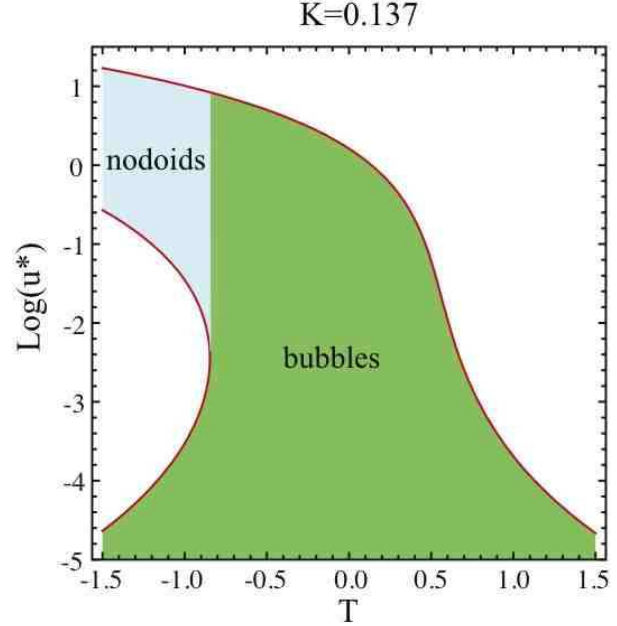


Fig. 8. The $t = 0$ slice through the T -surface at $K = 0.137$. Only two regimes are observed here; nodoids and bubbles for $T < T_1$ and bubbles only for $T > T_1$.

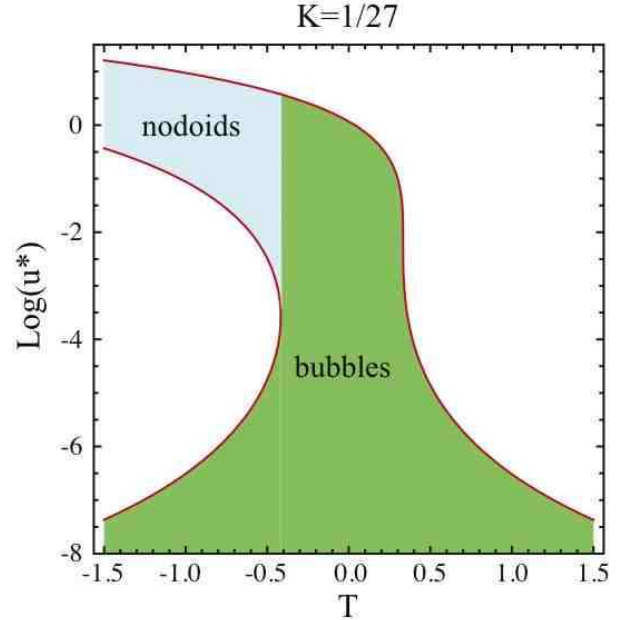


Fig. 9. The $t = 0$ slice through the T -surface at the critical point of $K = 1/27$. Compare Figs. 8 ($K > 1/27$) and 10 ($K < 1/27$).

Having deduced so much with so little, let's unravel what this implies for $P(u)$ in each case. We begin with the case $K > 1/27$, as $T_1 < 0$ is our only critical point and the situation is somewhat simpler. When $T < T_1$, there are three real roots and we will have two intervals of positivity, $(0, u_1)$ and (u_2, u_3) , and hence we have two distinct RAD surfaces, a closed bubble, which we call a “tiny bubble” and another surface we call a nodoid in analogy

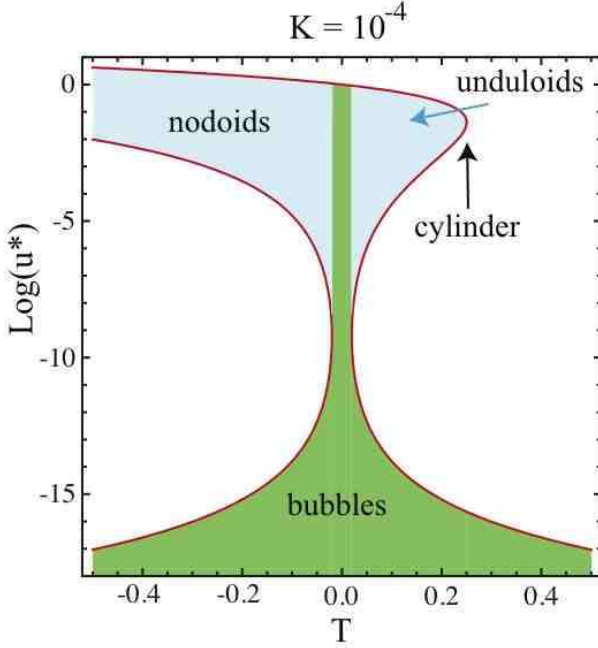


Fig. 10. The $t = 0$ slice through the T -surface with $K = 10^{-4}$ (qualitatively similar to Fig. 2, where $K = 10^{-2}$). There are four regimes, nodoids and bubbles for $T < T_1$, bubbles only for $T_1 < T < T_2$, unduloids and bubbles for $T_2 < T < T_3$, and bubbles only for $T > T_3$.

with the Delaunay surface since $T < 0$. T_1 corresponds to the point where the nodoids join with the tiny bubble (i.e. u_1 collides with u_2 and they move off the real axis). When $T > T_1$ there is one real root of u and we have one interval for which $P(u) > 0$, and the only valid integration interval is the one corresponding to the closed bubble, namely $(0, u_1)$. We note that this root is a continuation of u_3 from when $T < T_1$. In Fig. 8, $K = 1/27 + 0.1$, we show a semilog plot of the $t = 0$ slice of the T -surface depicting the space of surfaces.

On the other hand, if there are three critical points on the T -surface (when $0 < K < 1/27$), things become more complicated. Let the three critical values be then $T_1 < 0 < T_2 < T_3$. When $T < T_1$, $P(u)$ has three real roots, and so we have two distinct RAD surfaces, a “tiny bubble” and a nodoid again. T_1 corresponds to the point where the nodoids join with the tiny bubble. For $T_1 < T < T_2$, we have only a closed bubble solution, as now $P(u)$ has only one real root. We’ll sometimes call this the large bubble, to distinguish it from the tiny bubble solutions, though we will see (Fig. 11) that they may be taken to each other via a non-singular path surrounding the point $(T = 1/3, K = 1/27)$.

We have seen that for $T < 0$, there is always a portion of the contour on the negative branch of the T -surface, so the large bubble with $T < 0$ must be concave at $r = 0$, which we can verify by calculating d^2z/dr^2 at $r = 0$. For $T \geq 0$, the bubble is convex, and $T = 0$ is the free bubble case which we will consider in much more detail in section 4. In that case, we must consider d^4z/dr^4 at $r = 0$ to establish convexity.

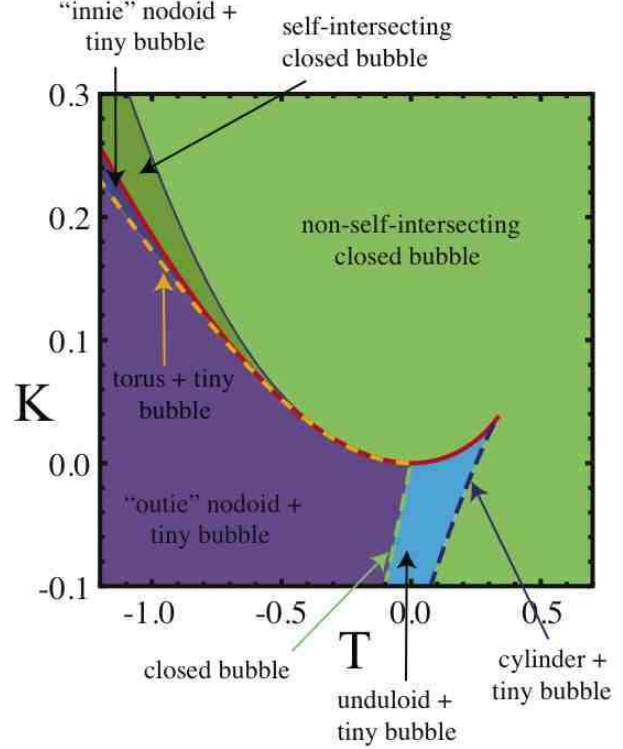


Fig. 11. RAD surface phase diagram, when $g(r) = 1/r^2$. The solid red curve and dotted dark blue curves separate regions with one RAD surface from regions with two RAD surfaces and are the curves defined by the vanishing of $Q_3(K, T)$ (eqn. 28). The period / height function for the surfaces diverges to $+\infty$ for $T < 0$ and $-\infty$ for $T > 0$ on the solid red line. The dotted green line is the line $T = K$. Together these curves are where the discriminant $Q(K, T) = 0$. The solid blue and dotted orange lines are calculated from the vanishing of the height $Z_1(T, K)$ and period $Z_3(T, K)$ (eqns. 33,32), respectively. Note that the non-self-intersecting closed bubble solutions can be divided into bubbles convex at $r = 0$ ($T \geq 0$) and concave at $r = 0$ ($T < 0$).

For $T_2 < T < T_3$, $P(u)$ has three real roots again, and we have both tiny bubbles and periodic non-self-intersecting RAD surfaces analogous to unduloids. At T_3 , the unduloids degenerate to a cylinder, though the tiny bubble is still there, and past T_3 there is only a tiny bubble solution. In Fig. 10 we show a semilog plot of the $t = 0$ slice of the T -surface for this case. Fig. 9 shows the limiting case $K = 1/27$, which behaves most like the $K > 1/27$ case. Since $T_2 = T_3$, the unduloids in the $0 < K < 1/27$ case are not visible. Therefore the change in character of the RAD surfaces as a function of T is controlled only by the critical point at T_1 .

In Fig. 11 we show a “phase diagram” in T and K of the types of surfaces possible. From this, we can see the “critical points” at $(T, K) = (1/3, 1/27)$ and $(0, 0)$ are where certain “first order” (branch cut) lines end. We conclude this section with a few sentences on the unphysical but mathematically enlightening case of $K < 0$. When $K < 0$, Q_3 only has one real root T_1 (actually the continuation of the root T_3 when $K > 0$), which lies between

the regime of unduloids and tiny bubbles and the regime of closed bubbles. However, now the $(K - T)$ factor of the complete discriminant Q of $P(u)$ becomes relevant. It defines a curious boundary between the nodoid and the unduloid. Though the line $T = K$ separates two regions for which there are two RAD surface solutions, the tiny bubble and a periodic surface (nodoid when $T < K$, unduloid on the $T > K$ side), on the line itself, the tiny bubble caps off the periodic surface to form only one solution, a larger closed bubble. This behavior generalizes the nodoid to sphere to unduloid transition at $T = 0$ for the Delaunay surfaces. This observation thus unifies the periodic surfaces somewhat. Below we will again concentrate on surfaces with $K > 0$, though our formulas are applicable to all K .

3 Shapes

We finally turn to the particulars of the allowed shapes as we explore the contours of constant T . When $n = 1$ the radicand in (23) is cubic in u and thus the integral may be evaluated in terms of elliptic functions:

$$\begin{aligned} z_3(r) &= \int_{r^2}^{u_3} \frac{(T+u)du}{2\sqrt{P(u)}} \\ &= \frac{T+u_1}{\sqrt{u_3-u_1}} F\left(\sqrt{\frac{u_3-r^2}{u_3-u_2}}, \sqrt{\frac{u_3-u_2}{u_3-u_1}}\right) \\ &\quad + \sqrt{u_3-u_1} E\left(\sqrt{\frac{u_3-r^2}{u_3-u_2}}, \sqrt{\frac{u_3-u_2}{u_3-u_1}}\right) \end{aligned} \quad (30)$$

where $F(\phi, k)$ and $E(\phi, k)$ are the elliptic integrals of the first and second kind, respectively, and the u_i are the roots of P . The domain of this function is $u_2 < r^2 < u_3$ when we are looking at nodoids and unduloids. For the large bubble case, $P(\tilde{u})$ has only one real root \tilde{u}_1 , so we must break this naming convention when interpreting the formula above by taking u_1, u_2 to be the complex conjugate roots and u_3 to be the real root. In this case, the domain is $0 < r^2 < \tilde{u}_1$. The tiny bubble shape can be expressed in this form as well:

$$\begin{aligned} z_1(r) &= \int_{r^2}^{u_1} \frac{(T+u)du}{2\sqrt{P(u)}} \\ &= \frac{T+u_1}{\sqrt{u_3-u_1}} F\left(\sqrt{\frac{u_3-r^2}{u_2-r^2}}, \sqrt{\frac{u_3-u_2}{u_3-u_1}}\right) \\ &\quad + \sqrt{u_3-u_1} E\left(\sqrt{\frac{u_3-r^2}{u_2-r^2}}, \sqrt{\frac{u_3-u_2}{u_3-u_1}}\right) \\ &\quad - \sqrt{\frac{(u_3-r^2)(u_1-r^2)}{u_2-r^2}} \end{aligned} \quad (31)$$

Here $0 < r^2 < u_1$. The integral could describe the closed bubble as well, but our choices of elliptic integrals here

turn out to be on the wrong branch for that case. For large $|T|$, the root of $P(u)$ is $u_1 \sim \frac{K^2}{T^2-2K} \sim K^2/T^2$. Since in this limit u_1 is small, the remainder of the radicand varies slowly in $u \in [0, u_1]$. Hence in this limit the bubble shape becomes spherical, $z_1(r) \approx -\frac{T}{|T|}\sqrt{u_1-r^2}$; the tiny and closed bubbles become spherical as $T \rightarrow \infty$.

In Fig. 12 we show some representative generating curves in the case $0 < K < 1/27$, specifically with $K = 0.01$. Note that as T increases we go from branches of nodoids which begin at $z = 0$ and end at some $z \neq 0$, to large bubbles which end at $r = 0$, and finally to branches of unduloids which also end at $z \neq 0$. The generating curves for $K = 0.55 > 1/27$ are depicted in Fig. 13 where we transition from nodoids to concave to convex bubbles as T grows. We may also analyze the behavior of the solutions as a function of T by considering the period function as we did for Delaunay surfaces:

$$\begin{aligned} Z_3 &= \int_{u_2}^{u_3} \frac{(T+u)du}{\sqrt{(u-u_1)(u-u_2)(u_3-u)}} \\ &= 2\frac{T+u_1}{\sqrt{u_3-u_1}} K\left(\sqrt{\frac{u_3-u_1}{u_3-u_2}}\right) \\ &\quad + 2\sqrt{u_3-u_1} E\left(\sqrt{\frac{u_3-u_1}{u_3-u_2}}\right) \end{aligned} \quad (32)$$

Z_3 only yields the periods for nodoids and unduloids, and the complete elliptic integrals are chosen so that their moduli satisfy $0 < k < 1$ when $P(u)$ has three real roots, so that the integral is real. For the tiny bubble, we have:

$$Z_1 = \int_0^{u_1} \frac{(T+u)du}{\sqrt{P(u)}} = 2z_1(0) \quad (33)$$

In the case of three roots Z_1 also gives the height of the closed bubble. In the large $|T|$ limit, since these bubbles become spherical, $Z_1 \sim 2r_1 = 2\sqrt{u_1} \sim -2T/K$, with the sign chosen to agree with that of Z_1 . The notations for Z_j and z_k are independent of each other, with j referring to the number of real roots required to exist for Z_j to make sense, and k referring to the upper limit of integration u_k .

In Fig. 14 we show the behavior of Z_3 and Z_1 for various values of K . The $K > 0$ period functions Z_3 and Z_1 both have divergences at $T = T_1$ and $T = T_2$; this is visible in the plot as vertical lines where three curves $Z_3(T < T_j)$, $Z_1(T < T_j)$, and $Z_1(T > T_j)$ join. On the phase diagram (Fig. 11), the divergences lie on the solid red line; the divergence to $+\infty$ at $T_1 < 0$ and $-\infty$ at $T_2 > 0$. Physically, this signals a loss of mechanical stability in these systems, as an “elastic modulus” of $dF_z/dz = dT/dZ$ goes to zero. From our discussion earlier, $T = T_1$ is where the nodoid and tiny bubble solutions merge. Fig. 15 illustrates this for $K = 0.01$ and $K = 0.55$. We can also think of this process as the tiny bubble “tearing off” as we increase the compression on a large bubble (decrease T) past T_1 .

The nodoids close to T_1 have the “loops outside” as shown in Fig. 17d, as opposed to the usual “loop inside” nodoids in the Delaunay surface case shown in Fig. 7b. In terms of Z_3 , we see that “innies” are when $Z_3 < 0$ and

“outies” are when $Z_3 > 0$. The period diverges at $T = T_1$ in Z_3 , which appears for all $K > 0$ but not $K = 0$. The fact that the divergence is positive guarantees a value of $T_{\text{torus}} < T_1 < 0$ where $Z_3 = 0$ and a torus appears. We show the tori at $K = 0.01$ and $K = 0.55$ in Figs. 17e,f. The curve $T_{\text{torus}}(K)$ is also drawn on the phase diagram (Fig. 11) as well. Note that T_{torus} for $K = 0.01$ is very close to T_1 and the generating curve for the $K = 0.55$ torus is quite close to circular. In fact, we find numerically that as $K \rightarrow \infty$, $T_{\text{torus}} \sim -3K - 2/3$ and the generating

curve approaches $\pm\sqrt{\frac{4}{9} - (r - \sqrt{3K})^2}$, a circular torus with ring radius $\sqrt{3K}$ and tube radius $2/3$. These length scales can be derived analytically by finding the first few terms in a series solution (in \sqrt{K}) for u_2 and u_3 , assuming the empirically derived behavior of T_{torus} .

Finally, we turn to the closed bubble solutions: as T grows from negative to positive, the bubbles change from concave to convex at $r = 0$, this follows from the expansion $z_1(r) = \frac{T}{2K}(u_1 - r^2) + \mathcal{O}(r^4)$. From the divergence in Z_1 at T_1 and T_2 , we know that the height of the bubble goes to infinity when it joins with the nodoid and unduloid. Closed bubbles with $Z_1 = 0$ are tangent to themselves at the origin, and so $Z_1(T, K) = 0$ forms the line between self-intersecting and non-self-intersecting bubbles (Fig. 11). We show concave bubbles with $K = 0.55$ in Figs. 17b,c, and a bubble close to T_2 with $K = 0.01$ in Fig. 17a. The splitting of such a protruding bubble into a tiny bubble and an unduloid is depicted in Fig. 16 when $K = 0.01$. We add that this shape is reminiscent of those found in Canham-Helfrich membrane models for vesicles [26].

Note that although the unduloids end at $T = T_3$, there is no indication in the period function; indeed, as with the pure Delaunay case, the cylindrical solution actually has a finite period as a limit of unduloids. Neither of the elliptic integrals making up the period function has any divergence at this point. Hence, in contrast to the behavior at T_1 and T_2 , the tiny bubble solution at T_3 is completely regular.

4 Free Bubbles

From this point forward we discuss only the $T = 0$ case of free bubbles. In future work we will start from these equilibrium shapes to study the dynamics of the nematic double bubble [7]. As before, we define $z = 0$ at the “equator”, where $dr/dz = 0$. We define $R = r(0)$ as the waist of the bubble. Specialized to $T = 0$ and $g(r) = 1/r^2$, (14) reads

$$p = \frac{2}{R} \left(1 + \frac{K}{R^2} \right) \quad (34)$$

As we argued, when $T = 0$ there is a closed bubble for all K . Accordingly, R will be analogous to the radius of this bubble. We define here the new dimensionless quantities $\hat{K} = \frac{K}{R^2}$ and $\hat{p} = pR = 2(1 + \hat{K})$. Our previous choice for dimensionless quantities had the advantage of removing p , but had the disadvantage that the $K \rightarrow \infty$ limit is

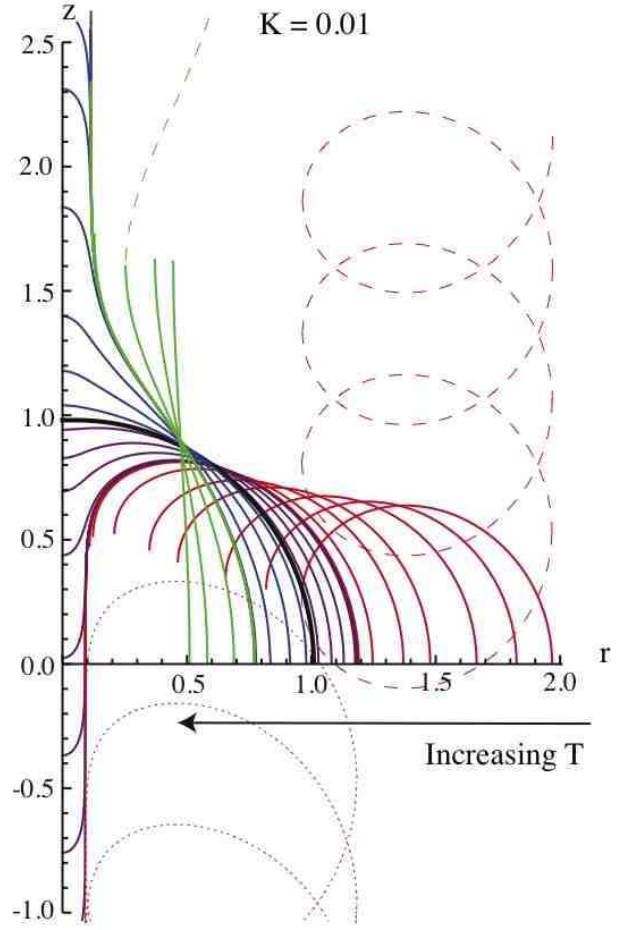


Fig. 12. Generating curves (for the nodoids, large bubbles, and unduloids) at $K = 0.01$. The surfaces are color-coded: nodoids are red, concave closed bubbles are purple, $T = 0$ is black, convex (at $r = 0$) bubbles are blue, and unduloids are green. Dashed curves show a few repeats of an “innie”, an “outie”, and an unduloid.

obscured; this turns out to be an important limit for dynamics. Our choice here represents a change in viewpoint. Instead of viewing p as a given parameter that we can remove via scaling, p is now a quantity which we calculate given R and K . These correspond to constant pressure versus constant size approaches, respectively. In these units, the first integral (13) determines the bubble shape via:

$$\begin{aligned} \frac{2z}{R} &= \int_{\frac{r^2}{R^2}}^1 \frac{\hat{p} u du}{\sqrt{4(u + \hat{K})^2 - \hat{p}^2 u^3}} \\ &= \int_{\frac{r^2}{R^2}}^1 \frac{(1 + \hat{K}) u du}{\sqrt{(u + \hat{K})^2 - (1 + \hat{K})^2 u^3}} \end{aligned} \quad (35)$$

We can factor the cubic in the radical to find that the only real root is at $u = 1$. This is consistent with our more general arguments (Fig. 11); when there are three critical points in T , $T = 0$ lies in the large bubble region, while when there is one critical point $T_1 < 0$, $0 = T > T_1$ is in the closed bubble region. Written in terms of the

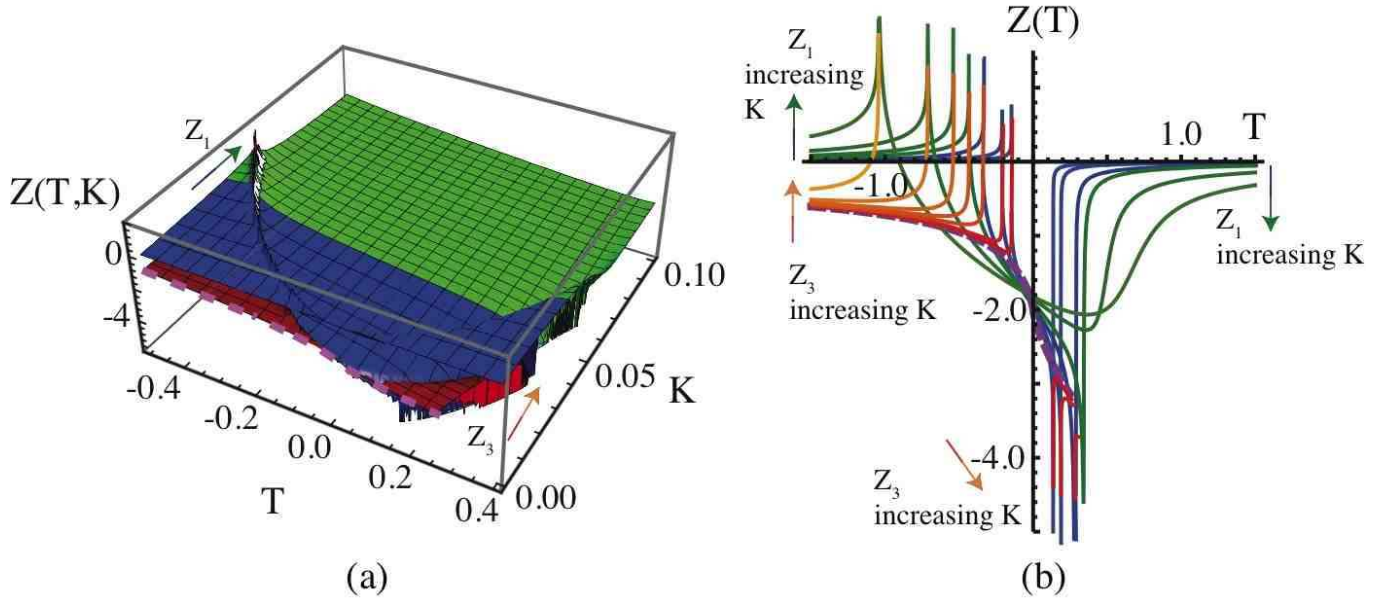


Fig. 14. The functions Z_3 and Z_1 , which give the period of unduloids and nodoids and the height of closed bubbles, respectively. (a) The period surface $Z(T, K)$. The Z_3 surface is red and the Z_1 surface with $K < 1/27$ is blue, and Z_3 with $K > 1/27$ is green. The single period function Z at $K = 0$ is the dashed and purple edge of the red Z_3 surface. The phase diagram (Fig. 11) gives a “top view” of this surface. (b) Constant K slices through the period surface. Again, Z_3 curves are red and orange, Z_1 curves are blue for $K < 1/27$ and green for $K > 1/27$, and $K = 0$ is the dashed purple curve.

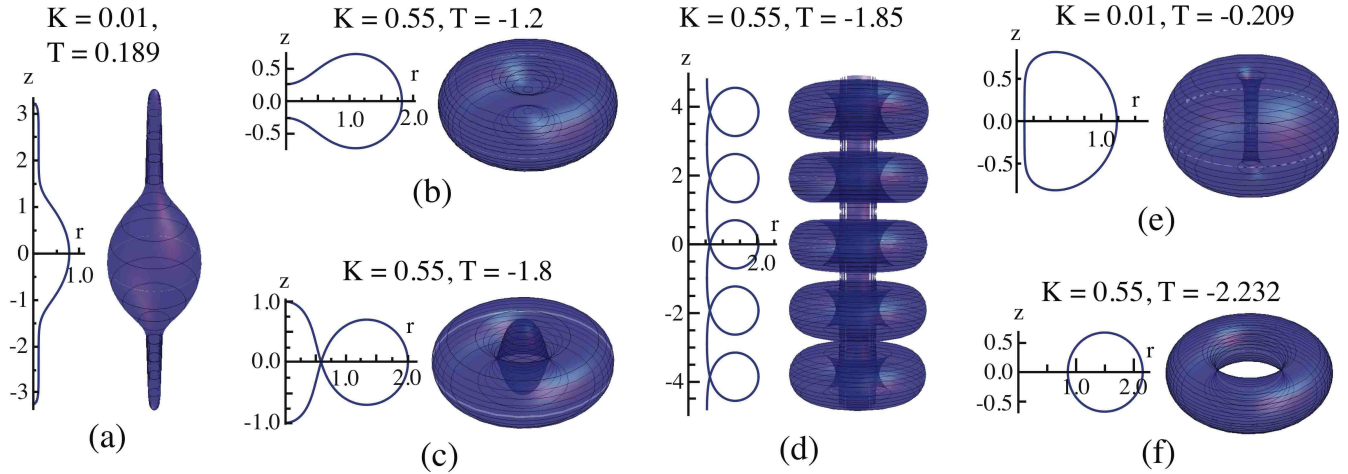


Fig. 17. From left to right: (a) A closed, protruding bubble at $K = 0.01$ with $T_2 = 10^{-7}$, where $T_2 = 0.1887$. Concave bubbles at $K = 0.55$ with $T = -1.2$ (b) and $T = -1.8$ (c). (d) An “outie” nodoid at $K = 0.55$ with $T = -1.85$; $T_1 = -1.848$ at this K . Tori at $K = 0.01$ (e) and $K = 0.55$ (f). For $K = 0.01$, $T_{\text{torus}} = T_1 - 4.48 \times 10^{-8}$ where $T_1 \approx -0.209$ and for $K = 0.55$, $T_{\text{torus}} = -2.232$ and $T_1 = -1.848$.

elliptic functions F and E , we have:

$$\begin{aligned} \frac{z(r)}{R} &= \frac{u_-}{\sqrt{1-u_-}} F \left(\sqrt{\frac{1-\frac{r^2}{R^2}}{1-u_+}}, \sqrt{\frac{1-u_+}{1-u_-}} \right) \\ &\quad + \sqrt{1-u_-} E \left(\sqrt{\frac{1-\frac{r^2}{R^2}}{1-u_+}}, \sqrt{\frac{1-u_+}{1-u_-}} \right) \quad (36) \\ u_{\pm} &= \frac{-\hat{K}}{2(1+\hat{K})^2} (2 + \hat{K} \pm i\sqrt{4\hat{K} + 3\hat{K}^2}) \end{aligned}$$

In Fig. 18 we show the generating curve for several values of \hat{K} . Note that the shape of the curve becomes more oblate as \hat{K} increases. Intuitively, this makes sense, as the K/r^2 term in the energy penalizes surfaces with more material close to the axis.

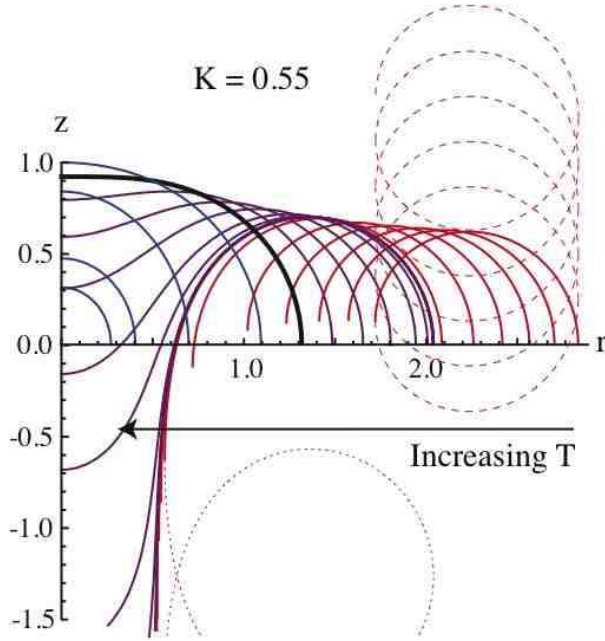


Fig. 13. Generating curves (for the nodoids and bubbles) at $K = 0.55$. Nodoids are red, concave closed bubbles are purple, $T = 0$ is black, convex (at $r = 0$) bubbles are blue. Dashed curves show a few repeats of an “innie” and an “outie”.

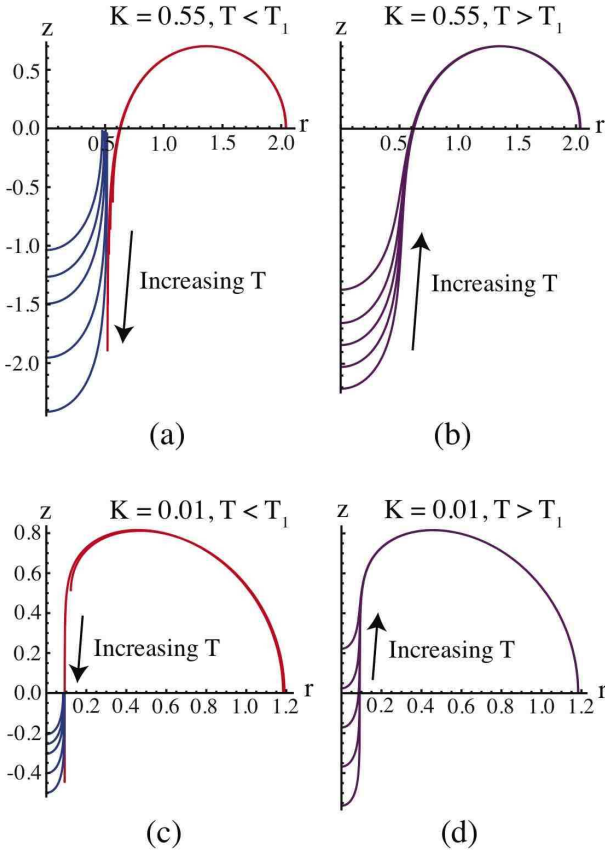


Fig. 15. The transition between nodoid and tiny bubble to large bubble for $K = 0.01$ ((a) and (b)) and $K = 0.55$ ((c) and (d)). The period of the nodoid and height of the bubbles diverge when the two surfaces join.

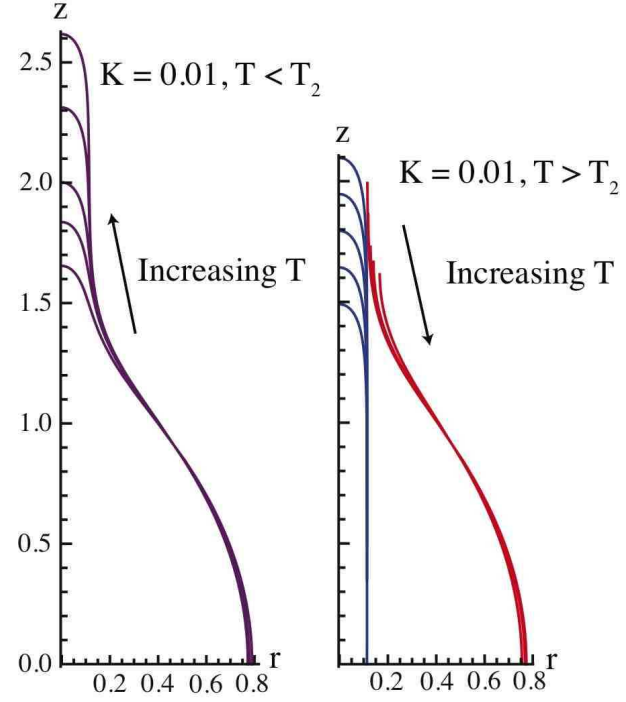


Fig. 16. The transition between large bubble to unduloid and tiny bubble for $K = 0.01$. Note the divergence again in the heights of the surfaces.

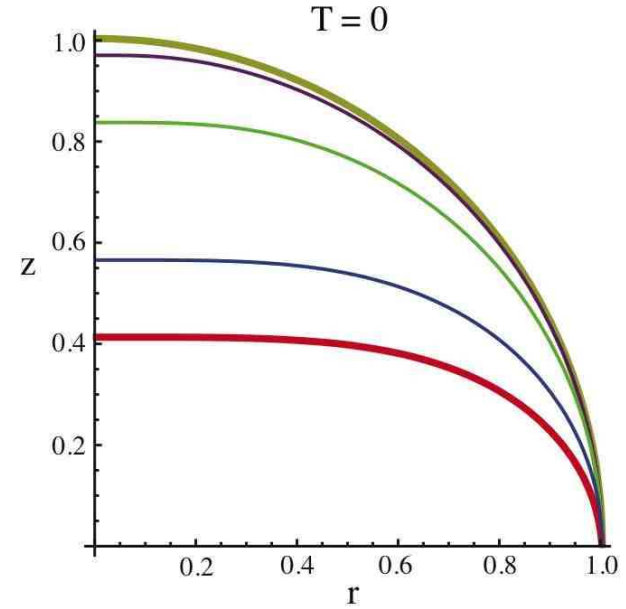


Fig. 18. Profile of free bubble ($T = 0$) for $\hat{K} = 0, 0.01, 0.1, 1, \infty$ from top to bottom. The limiting scale-invariant $\hat{K} = 0$ (gold) and $\hat{K} = \infty$ (red) are emphasized in bold.

4.1 Perturbative expansions

Though an expression in terms of elliptic integrals is compact and useful for plotting, we have garnered further insight into the shapes via perturbation for small \hat{K} . Starting with

$$\frac{2z}{R} = \int_{\frac{r^2}{R^2}}^1 \frac{\hat{p} du}{\sqrt{4(u + \hat{K})^2 - \hat{p}^2 u^3}} \quad (37)$$

we expand to find this to second order in \hat{K} :

$$\begin{aligned} \frac{2z}{R} = & 2\sqrt{1 - \frac{r^2}{R^2}} - \hat{K} \left(2 \ln \left[\frac{R}{r} + \sqrt{\frac{R^2}{r^2} - 1} \right] \right) \\ & + \hat{K}^2 \left(4 \ln \left[\frac{R}{r} + \sqrt{\frac{R^2}{r^2} - 1} \right] + \sqrt{\frac{R^2}{r^2} - 1} \right) \\ & + \mathcal{O}(\hat{K}^3) \end{aligned} \quad (38)$$

Away from $r = 0$, the first correction is negative, confirming that the surfaces flatten out with increasing \hat{K} . Note that the terms of order $\mathcal{O}(\hat{K})$ and above diverge at $r = 0$, indicating that the expansion is not uniformly convergent for all r . Examining (12), we see that the $\hat{K} \rightarrow 0$ limit is singular at $r = 0$ since the term with the highest power of $1/r$ drops out.

The $\hat{K} \rightarrow \infty$ limit does not suffer from this convergence issue. Expanding in powers of $\kappa \equiv \hat{K}^{-1}$, we find

$$\begin{aligned} \frac{2z}{R} = & \int_{\frac{r^2}{R^2}}^1 \frac{u du}{\sqrt{1 - u^3}} + \kappa \int_{\frac{r^2}{R^2}}^1 \frac{u(1 - u) du}{(1 - u^3)^{3/2}} \\ & + \kappa^2 \int_{\frac{r^2}{R^2}}^1 \frac{u^2(1 - u)^2(-2 - 2u + u^2) du}{2(1 - u^3)^{5/2}} \\ & + \mathcal{O}(\kappa^3) \end{aligned} \quad (39)$$

This expansion is regular for all $0 \leq r \leq R$ for the first few terms, and one can argue that this perturbation series is regular in κ and r since the singular point at $\hat{K} = 0, r = 0$ has now moved to $\kappa = \infty, r = 0$. Fortunately, these integrals are related to known functions (useful for plotting!):

$$\begin{aligned} \frac{2z}{R} = & \frac{2\sqrt{\pi}\Gamma(\frac{2}{3})}{\Gamma(\frac{1}{6})} - \frac{1}{3}B\left(\left(\frac{r}{R}\right)^6; \frac{2}{3}, \frac{1}{2}\right) \\ & + \kappa \left[\frac{2}{3\sqrt{1 - (\frac{r}{R})^6}} - \frac{4i\sqrt{\pi}\Gamma(\frac{11}{6})}{\Gamma(\frac{1}{3})} \right. \\ & \left. - \frac{2i}{5}\left(\frac{R}{r}\right)^5 {}_2F_1\left(\frac{5}{6}, \frac{3}{2}; \frac{11}{6}; \left(\frac{R}{r}\right)^6\right) \right] \\ & + \mathcal{O}(\kappa^2) \end{aligned} \quad (40)$$

where $B(z; a, b)$ denotes the incomplete Beta function and ${}_2F_1(a, b; c; z)$ denotes the standard hypergeometric series. The first term gives us the $\hat{K} \rightarrow \infty$ bubble shape, in other

words the shape of a bubble with only nematic elastic energy and no surface tension energy.

We have used these expansions to study the shape near the north and south poles at $r = 0$ and the equator at $r = R$. When $\hat{K} = 0$ the generating curve is a circle, quadratic near the poles and with a square-root cusp at the equator. However, for $\hat{K} \neq 0$, the behavior is quartic at $r = 0$: $z(r) = \frac{K+R^2}{4KR^3}r^4 - \mathcal{O}(r^6)$. The power of K in the denominator in the coefficient of the leading term explains why the expansion in powers of K is singular at $r = 0$. Near $r = R$, $z(r)$ is still a square root: $z(R - \ell) = \frac{(K+R^2)\sqrt{2R}}{\sqrt{3K^2+4KR^2+R^4}}\sqrt{\ell} - \mathcal{O}(\ell^{3/2})$. Thus, both expansions are valid there.

5 Conclusion

In the future, we will consider the dynamics of the two bubbles shown in Fig. 1. The two limits we studied here perturbatively control the two long-time, scale-invariant limits of the solutions. As discussed earlier, at finite K , the problem has two length scales, R and \sqrt{K} - as the value of $\hat{K} = \left(\frac{\sqrt{K}}{R}\right)^2$ changes, one or the other limit becomes more appropriate, thus as the length scale set by geometry R (e.g. by assuming an initial volume) becomes much smaller than \sqrt{K} through diffusion, we go to the $\hat{K} = \infty$ or “pure nematic” limit.

We were able to analyze this special case where the director was azimuthal and found the complete range of allowed shapes and topologies. Whether we can extend our method of analysis for longitudinal alignment or general alignment is an open question.

Acknowledgments

It is a pleasure to acknowledge useful and stimulating discussions with R.B. Kusner and V. Vitelli. This work was supported by NSF Grant DMR05-47230 and by gifts from L.J. Bernstein and H.H. Coburn.

References

1. J. A. F. Plateau, *Statique Expérimentale et Théorique des Liquides Soumis aux Seules Forces Moléculaires*, (Gauthier-Villard, Paris 1873); See also K. Brakke’s English translation available online at <http://www.susqu.edu/brakke/>
2. J. E. Taylor. *Annals of Mathematics*. **103**, (1976) 489-539
3. R. Lemlich, *Ind. En. Chem. Fundam.* **17**, (1978) 89.
4. A.J. Markworth, *J. Col. Int. Sci.* **107**, (1985) 569.
5. A. Monsalve and R.S. Schechter, *J. Col. Int. Sci.* **97**, (1984) 327.
6. M. Buchanan. arXiv:cond-mat/0206477, (2002).
7. B. G. Chen and R.D. Kamien, *in preparation*, (2008).
8. J. E. Avron, J. E. Taylor, R. K. P. Zia. *J. Stat. Phys.* **33**, (1983) 493. 421-470.
9. R. K. P. Zia and A. Gittis. *Phys. Rev. B* **35**, (1987) 5907-5909.

10. H. Wente. Pacific J. Math. **80**, (1980) 421-470.
11. M. Koiso and B. Palmer. Indiana U. Math. J. **54**, (2005) 1817-1852.
12. M. Koiso and B. Palmer. Pacific J. Math. **234**, (2008) 345-378.
13. T. C. Lubensky and F. Mackintosh. Phys. Rev. Lett. **67**, (1991) 1169-1172.
14. T. C. Lubensky and J. Prost. J. Phys. II France **2**, (1992) 371-382.
15. O-Y. Zhong-Can. Thin Solid Films **393**, (2001) 19-23.
16. V. Vitelli and D. R. Nelson. Phys. Rev. E **74**, (2006) 021711.
17. J. R. Frank and M. Kardar. Phys. Rev. E **77**, (2008) 041705.
18. H. Jiang, G. Huber, R.A. Pelcovits, T.R. Powers, Phys. Rev. E **76**, (2007) 021704.
19. V. Elser, *personal communication*.
20. P. G. de Gennes and J. Prost. *The Physics of Liquid Crystals*, 2nd ed. (Oxford University Press, Oxford 1995) 100-103.
21. F. Morgan. Rev. Mod. Phys. **79**, (2007) 821.
22. D. A. Dunmur, A. Fukuda and G. R. Luckhurst, ed. *Physical Properties of Liquid Crystals: Nematics*, (INSPEC, London 2001) 223 and 488.
23. N. Korevaar, R. Kusner and B. Solomon, J. Differential Geometry 30 (1989), 465-503.
24. K. Kenmotsu. *Surfaces with Constant Mean Curvature*. trans by Katsuhiko Moriya. Translations of Mathematical Monographs 221. AMS (2003). (American Mathematical Society, Providence 2003) 39-52.
25. J. Eells. Math. Intel. **9**, (1987) 53-57.
26. T.R. Powers, G. Huber and R.E. Goldstein. Phys. Rev. E **65**, (2002) 041901.